Optimization-Based Estimation and Model Predictive Control for High Performance, Low Cost Software-Defined Power Electronics

Liwei Zhou, *Member, IEEE*, Michael Eull, *Member, IEEE*, and Matthias Preindl, *Senior Member, IEEE*

***Abstract*—A combined optimization-based estimation (OBE)-model predictive control (MPC) technique is developed to improve the dynamic performance of a reconfigurable LC-based power module with lower cost and less noise/oscillation. The developed OBE-MPC technique and the corresponding power module are based on a software-defined power electronics concept that can be reconstructed as different topologies and applied to various load/source applications, e.g., dc/dc converters, dc/ac single/three-phase grid-connected inverters, and ac/ac motor traction inverter to improve the energy conversion performance. The software-defined power electronics are designed in a generalized way by manipulating a different number of OBE-MPC power modules with holistic high-level control functions for wide applications. Symmetrically mirrored to the MPC, the OBE is configured as a constrained finite time optimal estimation (CFTOE) problem to solve the quadratic cost function based on the past sampling information. With the designed OBE, the sensor count is reduced with less noise/oscillation. And the highly accurate OBE contributes to the correction of possible modeling parametric or sampling errors. The integration of OBE-MPC algorithms improves both the steady-state and dynamic performances with less noise/oscillation, more robust transient behavior, and higher control bandwidth. The explicit design of OBE-MPC algorithms makes it possible to implement the functions on a low-cost DSP. Also, the state-space modeling of OBE-MPC for the LC-based power module is immune to the output side unknown inductance, which further improves the parametric accuracy. The proposed methods have been validated experimentally.**

***Index Terms*—Dynamic performance, grid-connection, model predictive control (MPC), motor drives, optimization-based estimation (OBE), software-defined power electronics.**

I. Introduction

THE power quality, dynamic performance, and cost of the power converters are three key aspects for the evaluation of an energy conversion system. For the power quality, a high-order filter, such as LC or LCL, can be applied to the converter to filter out the harmonics. However, there exists resonance oscillation in high-order filter systems, which could result in stability issues. Some passive/active damping techniques have been studied to deal with the resonance by either introducing extra passive components or adding extra ADC sampling information with the corresponding integral calculation into the control loop. For the dynamic performance, higher control bandwidth, or more advanced control techniques could contribute to the improvement of transient behavior. However, higher control bandwidth requires more cost on the controller's computation capability. Advanced control methods, such as MPC, can also promote the dynamic performance. However, MPC is typically implemented based on solving the constrained optimization problem, which may still require more computation resources. For the cost reduction of power converters, sensorless control is one of the most straightforward ways to save components on the sensor count and reduce the related hardware cost.

The state estimator is a typical technique to improve the power quality and reduce the cost for power converters [1], [2]. In a power electronics system, the voltage/current samplings are crucial parameters that could directly influence the performance of power control. Due to the hardware limitations, e.g., EMI noise from the high power traces, and measurement error, of the sensing circuits, the control system could be interfered by the sampling noise or oscillation. The state estimation can be a substitute for part of the ADC sampling information to reduce the noise/oscillation from the corresponding sensors [3], [4]. Also, the state estimation contributes to the reduction of sensor count and system cost. Conventionally, the Luenberger Observer is a basic state estimation method and has been widely used in the industrial applications, which is a linear type of observer and can be easily implemented in the digital control systems [5], [6]. Besides the Luenberger Observer, optimization-based estimation (OBE) is a more advanced estimation approach that leverages a series of past measurements to derive the desired accurate state values by solving a constrained optimization problem [7], [8]. The OBE has been verified for the application of virtual flux estimation in the electric machine to estimate the position and speed [9], [10], [11]. Few studies have been focusing on the applications of different topologies to be interfaced with wider ranges of load/source. Also, the computation

Manuscript received 31 March 2022; revised 29 June 2022; accepted 19 August 2022. Date of publication 30 August 2022; date of current version 10 October 2022. This work was supported in part by NSF CAREER award under Grant 1653574. Recommended for publication by Associate Editor Santanu Kapat. *(Corresponding author: Matthias Preindl.)*

Liwei Zhou and Matthias Preindl are with the Electrical Engineering, Columbia University, New York, NY 10027 USA (e-mail: lz2575@columbia.edu; matthias.preindl@gmail.com).

Michael Eull is with the Electronic and Electrical Engineering, University of Strathclyde, G1 1XQ Glasgow, U.K. (e-mail: we2148@columbia.edu).

Color versions of one or more figures in this article are available at https://doi.org/10.1109/TPEL.2022.3202863.

Digital Object Identifier 10.1109/TPEL.2022.3202863

burden for the OBE on low-cost DSP is a crucial topic that needs to be addressed for the popularization of the technique. This article develops a general explicit OBE-MPC method for power modules that could be applied to various types of power converters with different load/source interfaces on a low-cost DSP.

Model predictive control (MPC) is an option for the promotion of dynamic performance and resonance damping, especially in high-order filter system [12], [13], [14]. Different from the conventional proportional-integral (PI) control, the MPC has been validated to have the advantages of better dynamic performance, including less rise time, overshoot, and oscillation during transient [15], [16]. [17] demonstrated the applications of the predictive control method with the corresponding merits of switching frequency reduction and output distortion attenuation. Also, the following three perspectives of conclusions have been drawn in this article, including:

1) MPC can derive the optimal results at a low switching frequency range;
2) high-frequency state variable sampling updates are not necessary for predictive control;
3) complicated modeling is not necessary for predictive control.

Several MPC algorithms have been studied in the field of power converters for motor traction or grid-connection [18], [19], [20], [21]. However, the combination of MPC and OBE for general application and low-cost implementation purposes has not been addressed in detail. The MPC and OBE are actually two symmetrical algorithms in the time series where OBE is focusing on the past sampling information and MPC is for the future steps. This article integrates the OBE and MPC on a generalized power module, which could be applied to various interfaced applications without consuming high computation burden on the controller.

For the modularization concept, power electronics building block (PEBB) has been proposed to standardize the hardware components for stackable energy conversion systems [22], [23], [24]. The PEBB concept is more focused on the physical components design to generalize the hardware power modules with extensible voltage/current capacity. Accordingly, in a PEBB system, the number of power blocks is mainly targeted for the desired power rating instead of various interfaced applications. On the contrary, some studies have also developed power electronics control architectures in a high-level perspective to cover various applications [25], [26], [27], [28]. This type of idea addresses more on the holistic interfaced control functions. The software-defined power electronics concept in this article basically combines the characteristics of hardware stackability and software reconfigurability. For the hardware stackability, the generalized power module can be physically connected in parallel for desired power rating based on the inspiration of the PEBB concept. For the software reconfigurability, the high-level controller can manage the desired number of power modules with the corresponding control functions based on the interfaced applications. And the OBE and MPC algorithms are configured for each local controller to estimate and stabilize the state variables. The local controller is necessary for implementing the OBE and MPC in each module since it is difficult to execute the optimization-based algorithms in a holistic way especially when the interfaced applications require a multiphase circuitry topology.

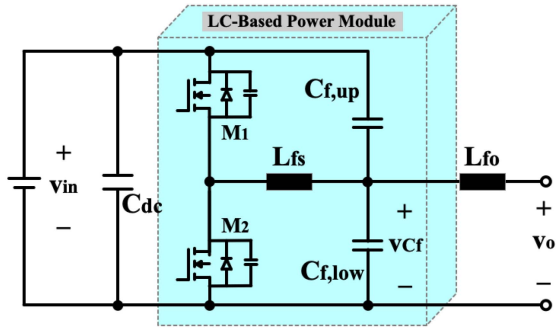

Fig. 1. LC-based power module with output side inductor.

The contributions of this article can be summarized in the following four aspects:

1) OBE-MPC algorithms are designed for a reconfigurable LC-based power module;
2) software-defined multilayer control structure is developed with high-level control functions and local level OBE-MPC power modules;
3) three types of interfaced applications have been validated, including dc/dc, single/three-phase dc/ac grid and motor traction;
4) proposed control and estimation methods show high performances in steady-state and transient modes.

This article is organized as follows. First, the state-space modeling of an LC-based power module is analyzed for the implementation of OBE-MPC as the generalized module of the software-defined power electronics. Second, the explicit OBE-MPC algorithms are designed with the corresponding general theories and implementation details. Also, the explicit working principle for reducing the computation burden on low-cost DSP has been illustrated. Third, based on the developed OBE-MPC equipped power module, various types of topologies and interfaced applications, including dc/dc converters, dc/ac single/three-phase grid-connected inverters, and motor traction inverters are demonstrated with the corresponding control diagrams based on the generalized software-defined power electronics concept. Finally, the proposed OBE-MPC technique for different applications has been experimentally validated to show its merits.

II. State-Space Modeling

The state-space modeling of the LC-based power module is analyzed in this section. The circuitry diagram of the basic LC power module is shown Fig. 1, which consists of upper/lower switches M_1 and M_2, switch side inductor L_{fs}, upper/lower output capacitors $C_{f,\text{up}}$ and $C_{f,\text{low}}$. An output side inductor L_{fo}, can also be connected to formulate an LCL converter. The desired number of introduced basic LC-based power modules can be connected and reconfigured to formulate different types of topological applications, such as multiphase dc/dc or dc/ac converters.

The state-space equations for the LC-based power module can be expressed as

$$\dot{i}_{Lfs}(t) = -\frac{1}{L_{fs}} v_{Cf}(t) + \frac{v_{\text{in}}}{L_{fs}} d(t) \tag{1a}$$

$$\dot{v}_{Cf}(t) = \frac{1}{C_f} i_{Lfs}(t) - \frac{1}{C_f} i_{Lfo}(t) \tag{1b}$$

$$\dot{i}_{Lfo}(t) = \frac{1}{L_{fo}} v_{Cf}(t) - \frac{1}{L_{fo}} v_o(t) \tag{1c}$$

where L_{fs}, C_f, and L_{fo} are the switch side inductor, output capacitor, and output side inductor, respectively. i_{Lfs}, v_{Cf}, i_{Lfo}, and v_o are the switch side inductor current, output capacitor voltage, output side current, and output voltage, respectively.

For the convenience of implementing the control algorithm in a low-cost DSP, the continuous state-space equations can be transformed into the discrete format as shown in the following:

$$i_{Lfs}(k+1) = i_{Lfs}(k) - \frac{T_s}{L_{fs}} v_{Cf}(k) + \frac{v_{\text{dc}} T_s}{L_{fs}} d(k) \tag{2a}$$

$$v_{Cf}(k+1) = \frac{T_s}{C_f} i_{Lfs}(k) + v_{Cf}(k) - \frac{T_s}{C_f} i_{Lfg}(k) \tag{2b}$$

$$i_{Lfo}(k+1) = i_{Lf0}(k) + \frac{T_s}{L_{fo}} v_{Cf}(k) - \frac{T_s}{L_{fo}} v_o(k) \tag{2c}$$

where T_s represents the time period of control interrupt in the DSP. The OBE-MPC algorithms are designed based on the discrete-time state-space modeling of the basic LC type of power module to formulate different applications of converter, e.g., single/three-phase dc/ac inverters, and multiphase dc/dc converters.

III. Estimation and Control

The proposed integrated OBE-MPC method for LC-based power module is analyzed in this section. These two advanced techniques are all configured by solving the constrained finite time optimization problems to increase the modeling/sampling accuracy, reduce the hardware cost, enhance the antinoise capability, and improve the steady-state/dynamic performances. These two techniques, OBE and MPC, are integrated based on a monolithic state-space model of LC power module by dealing with two sets of ADC sampling data. The two sets of sampling data for OBE and MPC are symmetric in time sequences for the past and future, respectively.

A. Optimization-Based Estimation

Different from the traditional Luenberger observer, OBE is designed to solve a constrained finite time optimal estimation (CFTOE) problem that requires a sequence of past sampling information. The general theory and the implementation for the LC-based power module are analyzed in this section.

1) General Theory of OBE: For the general applications of OBE in power converters, a theoretical model for the state-space system should be first built in a general way as follows:

$$x(k+1) = f(x(k), u(k)) + e_p(k) \tag{3a}$$

$$y(k+1) = g(x(k)) + e_m(k) \tag{3b}$$

where $x(k) \in \mathcal{X} \subseteq \mathbb{R}$ is the state variable vector, $u(k) \in \mathcal{U} \subseteq \mathbb{R}$ is the input variable vector, $y(k) \in \mathcal{Y} \subseteq \mathbb{R}$ represents the output variable vector, $e_p(k) \in \mathcal{E}_p \subseteq \mathbb{R}$ is the unknown processing disturbance, and $e_m(k) \in \mathcal{E}_m \subseteq \mathbb{R}$ is the unknown measurement noise.

The OBE algorithm is derived by solving the CFTOE problem. Thus, based on the general state-space equations in (3), a cost function can be configured to optimize the estimation values of the state variable vector, $x(k)$, by leveraging a series of past measurement of output variable vector, $y(k)$. The cost function can be generally expressed as

$$\underset{\hat{x}(M),\ldots,\hat{x}(0)}{\operatorname{argmin}} \sum_{k=M}^{-1} e_{p,k}^T \mathbf{Q}_E e_{p,k} + \sum_{k=M}^{0} e_{m,k}^T \mathbf{R}_E e_{m,k} + e_{x,M}^T \mathbf{P}_E e_{x,M} \tag{4}$$

and the constraints are followed as:

$$\text{s.t. } e_{p,k} = f(\hat{x}(k), u(k)) - \hat{x}(k+1) \in \mathcal{E}_p \tag{5a}$$

$$e_{m,k} = g(\hat{x}(k)) - y(k) \in \mathcal{E}_m \tag{5b}$$

$$e_{x,k} = \hat{x}_M - x(E) \tag{5c}$$

$$\hat{x}(k) \in \mathcal{X} \tag{5d}$$

where $k < 0$ in (4) and (5) means the information derived from the past instants. The weighing matrices $\mathbf{Q}_E$ and $\mathbf{R}_E$ provide the penalties on processing disturbance and measurement noise, respectively. The matrix $\mathbf{P}_E$ is defined as the arrival cost, which is a basic term in OBE that connects the properties between the finite time estimators and the full information observers. The arrival cost term is used to summarize the past data, which have not been explicitly taken into account in the cost function. Also, the arrival cost term is leveraged to make sure of the stability, robustness, and convergence.

2) Implementation of OBE for LC-Based Power Module: The OBE method is applied to the LC-based power module for the optimal estimation. Considering the huge current ripple on the switch side inductor current measurement i_{Lfs} and the challenges to accurately sampling the averaged i_{Lfs}, the OBE is designed for per phase power module to provide more accurate switch side inductor current estimation and noise rejection for the MPC controller. The main purposes of the state estimator are following:

1) to avoid inaccuracy of inductor current sampling with high current ripple;
2) to improve the antinoise capability for better control performance;
3) to reduce the sensor cost.

The OBE is implemented by solving the CFTOE problem to derive the optimal estimated values of switch side inductor current $\hat{i}_{Lfs}$, capacitor voltage $\hat{v}_{Cf}$, and grid side inductor current $\hat{i}_{Lfo}$, with the samplings of capacitor voltage v_{Cf}, and grid side inductor current i_{Lfo}. The state-space equations for the discrete-time OBE can be expressed in the standard matrix format of

$$\hat{X}_{k+1} = A_E \hat{X}_k + B_E u_k \tag{6a}$$

$$\hat{Y}_k = C_E \hat{X}_k + D_E u_k \tag{6b}$$

where the variables and matrices for OBE represent

$$A_E = \begin{bmatrix} 0 & -\frac{T_s}{L_{fs}} & 0 \\ \frac{T_s}{C_f} & 0 & -\frac{T_s}{C_f} \\ 0 & 0 & 0 \end{bmatrix}, B_E = \begin{bmatrix} \frac{T_s}{L_{fs}} \\ 0 \\ 0 \end{bmatrix} \tag{7a}$$

$$C_E = \begin{bmatrix} 0 & 1 & 0 \\ 0 & 0 & 1 \end{bmatrix}, D_E = \begin{bmatrix} 0 \\ 0 \end{bmatrix} \tag{7b}$$

$$\hat{X}_k = \begin{bmatrix} \hat{i}_{Lfs}(k) \\ \hat{v}_{Cf}(k) \\ \hat{i}_{Lfo}(k) \end{bmatrix}, \hat{Y}_k = \begin{bmatrix} \hat{v}_{Cf}(k) \\ \hat{i}_{Lfo}(k) \end{bmatrix}. \tag{7c}$$

Based on the OBE state-space equations in (6), the OBE solves for the optimal estimated state variable sequence of $\hat{X}_M, \ldots, \hat{X}_0$ with the known past measurement sampling sequence of $Y_M, \ldots, Y_0$ and input variable sequence of $u_M, \ldots, u_{-1}$. The cost function of the OBE optimization problem is composed of the following two parts.

1) Minimization of error between state (6a) and estimated state variable $\hat{X}_{j+1}$, which can be expressed as

$$e_{X,k} = (A_E \hat{X}_k + B_E u_k) - \hat{X}_{k+1}. \tag{8}$$

(2) Minimization of error between state (6b) and measured sampling output variable Y_j, which can be expressed as

$$e_{Y,k} = (C_E \hat{X}_k + D_E u_k) - Y_k. \tag{9}$$

Thus, the OBE cost function for the CFTOE optimization can be expressed as

$$\min \sum_{k=M}^{-1} e_{X,k}^T Q_E e_{X,k} + \sum_{k=M}^{0} e_{Y,k}^T R_E e_{Y,k} \tag{10}$$

where Q_E and R_E represent the weighing factor matrices of the penalties that are implemented on the state variables and output variables, respectively.

The constraints of the OBE controller can be expressed as

$$e_{X,k} = (A_E \hat{X}_k + B_E u_k) - \hat{X}_{k+1} \in \mathcal{E}_{\mathcal{X}} \tag{11}$$

$$e_{Y,k} = (C_E \hat{X}_k + D_E u_k) - Y_k \in \mathcal{E}_{\mathcal{Y}} \tag{12}$$

$$\begin{bmatrix} -I_{Lfs,\max} \\ 0 \\ -I_{Lfo,\max} \end{bmatrix} \le \hat{X}_k \le \begin{bmatrix} I_{Lfs,\max} \\ v_{\text{in}} \\ I_{Lfo,\max} \end{bmatrix} \tag{13}$$

$$\begin{bmatrix} 0 \end{bmatrix} \le u_k \le \begin{bmatrix} v_{\text{in}} \end{bmatrix} \tag{14}$$

$$\begin{bmatrix} 0 \\ -I_{Lfo,\max} \end{bmatrix} \le Y_k \le \begin{bmatrix} v_{\text{in}} \\ I_{Lfo,\max} \end{bmatrix}. \tag{15}$$

For the purpose of reducing the OBE computation burden on a low-cost DSP controller, the CFTOE optimization problem is solved explicitly by generating a piecewise affine function, as shown in Fig. 3(a). The specific implementing process of explicit OBE mechanism in Fig. 3(a) is demonstrated in Fig. 4. The state-space equations of (6) and the constraints of the LC-based power module dynamic system are built offline to generate an online search tree and feedback law for the OBE optimization. In each estimation implementing time period, the active region r, is searched with the matrices $H_{r,E}$ and $K_{r,E}$. Then, in each of the specific active regions, the corresponding feedback law

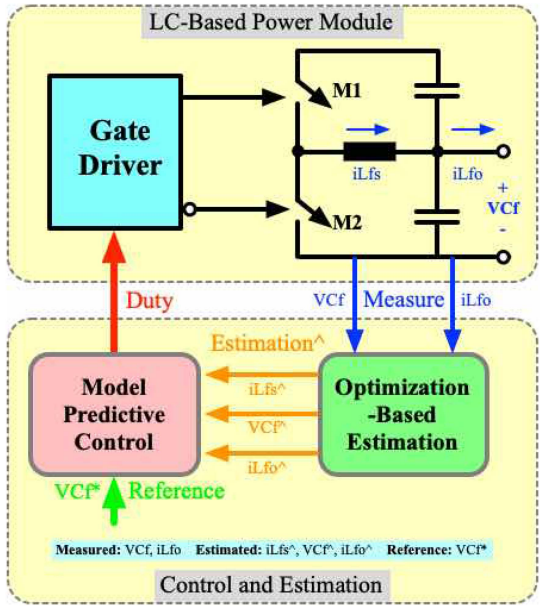

Fig. 2. OBE-MPC control diagram of LC-based power module.

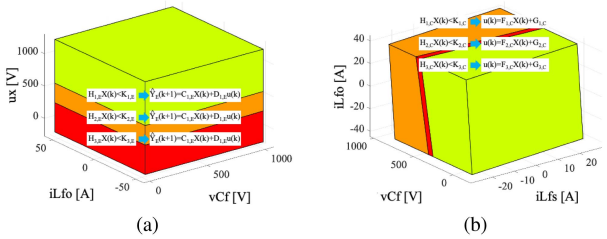

Fig. 3. (a) OBE and (b) MPC partitions for explicit implementations in DSP.

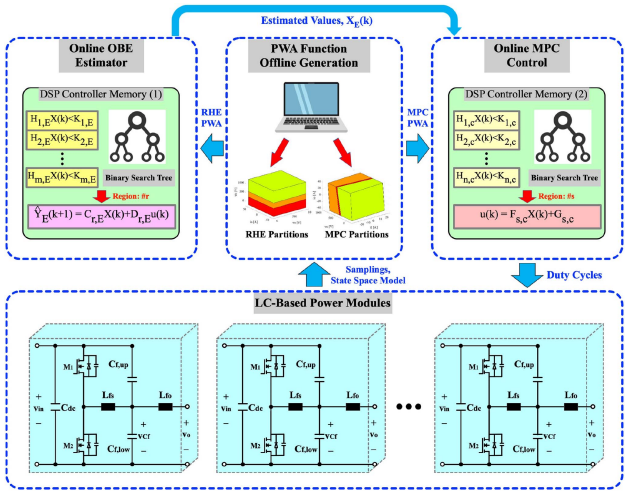

Fig. 4. Explicit implementation of OBE and MPC in DSP controller.

matrices $C_{r,E}$ and $D_{r,E}$, are applied to calculate the optimal output values $\hat{Y}_k$, with the estimation horizon. Different colored regions in Fig. 3(a) represent various piecewise affine feedback laws based on the measured variables.

For the real-time algorithm implementation, a binary search tree can find the optimal output values based on the updated state values of inductor current/output voltage [29]. Leveraging the

MultiParametric Toolbox from [30], the explicit OBE avoids the time-consuming online optimization process, thus it is suitable for high-frequency estimation. The binary search tree utilizes the theory in [29] by following a sequential search through the polyhedral regions of the partitions in Fig. 3 to find the optimal solution to the constrained optimization problem. For a clearer form of display, the colored areas of the generated piecewise affine region block with the state variables of i_{Lfs}, v_{Cf}, and i_{Lfo} in Fig. 3(a) represent the m regions for OBE to search and optimize according to the feedback law.

B. Model Predictive Control

1) General Theory of MPC: For the general applications of MPC in power converters, (3) is applied for the theoretical model of the state-space system. The MPC algorithm is derived by solving the constrained finite time optimal control (CFTOC) problem. Thus, based on the general state-space equations in (3), a cost function can be configured to minimize the tracking error between the state variable vector $x(k)$, and the references $\overline{x}(k)$, by predicting a series of the future input variable $u(k)$. The cost function can be generally expressed as

$$\underset{\substack{x(1),\ldots,x(N)\\ u(1),\ldots,u(N-1)}}{\operatorname{argmin}} \sum_{k=0}^{N-1} e_{x,k}^T \mathbf{Q}_C e_{x,k} + \sum_{k=0}^{N-1} e_{u,k}^T \mathbf{R}_C e_{m,k} + e_{u,N}^T \mathbf{P}_C e_{x,N} \tag{16}$$

and the constraints are followed as:

$$\text{s.t. } e_{x,k} = \overline{x}(k) - x(k) \tag{17a}$$

$$e_{u,k} = u(k) - u(k-1) \tag{17b}$$

$$x(k) \in \mathcal{X} \tag{17c}$$

$$u(k) \in \mathcal{U} \tag{17d}$$

where $k > 0$ in (16) and (17) means the information are expected for the prediction of the future instants. The weighing matrices $\mathbf{Q}_C$ and $\mathbf{R}_C$ provide the penalties on the tracking errors and control input variations, respectively. The matrix $\mathbf{P}_C$ is defined as the terminal cost, which is a basic term in MPC that connects the properties between the finite time MPC and the infinite time LQR. The terminal cost is used to make sure of the stability, robustness, and convergence.

2) Implementation of MPC for LC-Based Power Module: For the purpose of improving the dynamic performance, an explicit MPC method is designed for the per phase switch side capacitor voltage and inductor current control by solving the CFTOC problem. The switch side inductor currents are also regulated with the MPC by adjusting the weighing factor between i_{Lfs} and v_{Cf}. The benefits to configure the MPC (also OBE) for each of the LC-based power module instead of regarding multiphase power modules as a whole circuitry application for the algorithm implementation can be concluded as follows:

1) state-space matrix of LC per phase is simple with lower order to implement the offline piecewise affine optimization code in a less costly DSP controller;
2) for ac interface applications, the time-varying angular speed term ω in dq reference frame can be omitted in the explicit MPC state-space matrix for the offline optimization calculation;
3) per phase MPC for LC is more flexible for a modular design perspective to extend the paralleled phase number and other topologies, e.g., dc/dc, single-phase dc/ac converters.

For the MPC implementation, in every control period, the MPC controller receives the measured switch side inductor current i_{Lfs}, capacitor voltage v_{Cf}, output side current i_{Lfo}, from OBE of the optimal estimations and capacitor voltage reference v_{Cf}^* from the cascaded controller or manual setup. An offline generated piecewise affine search tree is applied to derive the optimal duty cycle for the explicit MPC. The state equations of switch side LC filter can be expressed as

$$i_{Lfs}(k+1) = i_{Lfs}(k) - \frac{T_s}{L_{fs}} v_{Cf}(k) + \frac{v_{\text{in}} T_s}{L_{fs}} d(k) \tag{18a}$$

$$v_{Cf}(k+1) = \frac{T_s}{C_f} i_{Lfs}(k) + v_{Cf}(k) - \frac{T_s}{C_f} i_{Lfo}(k). \tag{18b}$$

For the flexibility of implementing the explicit MPC and the convenience of experimentally adjusting the dc bus voltage during test, the last term of (18), $v_{in}d(k)$, can be replaced by the phase leg output voltage $v_x(k)$. The state-space model for MPC can be expressed in the standard matrix format of

$$X_{k+1} = A_C X_k + B_C u_k + E_C e_k \tag{19}$$

where the variables and matrices for MPC control represent

$$A_C = \begin{bmatrix} 1 & -\frac{T_s}{L_{fs}} \\ \frac{T_s}{C_f} & 1 \end{bmatrix}, B_C = \begin{bmatrix} \frac{T_s}{L_{fs}} \\ 0 \end{bmatrix}, E_C = \begin{bmatrix} 0 \\ -\frac{T_s}{C_f} \end{bmatrix} \tag{20a}$$

$$X_k = \begin{bmatrix} i_{Lfs}(k) \\ v_{Cf}(k) \end{bmatrix}, u_k = \begin{bmatrix} v_{in} d(k) \end{bmatrix}, e_k = \begin{bmatrix} i_{Lfo}(k) \end{bmatrix}. \tag{20b}$$

In the MPC formulation, the inductor current/capacitor voltage references can be defined as $\bar{X}$, and the tracking errors between the measurement and the references are expressed as $\tilde{X}$ which are composed of

$$\bar{X}_k = \begin{bmatrix} i_{Lfs,\text{ref}}(k) \\ v_{Cf,\text{ref}}(k) \end{bmatrix}, \tilde{X}_k = \begin{bmatrix} i_{Lfs,\text{ref}}(k) - i_{Lfs}(k) \\ v_{Cf,\text{ref}}(k) - v_{Cf}(k) \end{bmatrix}. \tag{21}$$

Thus, the cost function includes two terms

$$\min \sum_{k=0}^{N_c} \tilde{X}_k^T Q_C \tilde{X}_k + \sum_{k=0}^{N_p - 1} \triangle u_k^T R_C \triangle u_k. \tag{22}$$

For the penalties of the MPC cost function, Q_C and R_C represent the weighing factor matrices that are implemented on the state values and input values, respectively.

The constraints of the MPC controller can be expressed as

$$\tilde{X}_{k+1} = A\tilde{X}_k + Bu_k + Ee_k \in \mathcal{X} \tag{23}$$

$$\triangle u_k = u_k - u_{k-1} \in \mathcal{U} \tag{24}$$

$$\begin{bmatrix} -I_{Lfs,\max} \\ 0 \end{bmatrix} \le X_k \le \begin{bmatrix} I_{Lfs,\max} \\ v_{\text{in}} \end{bmatrix} \tag{25}$$

$$\begin{bmatrix} 0 \end{bmatrix} \le u_k \le \begin{bmatrix} v_{\text{in}} \end{bmatrix} \tag{26}$$

$$\begin{bmatrix} -I_{Lfo,\max} \end{bmatrix} \le e_k \le \begin{bmatrix} I_{Lfo,\max} \end{bmatrix}. \tag{27}$$

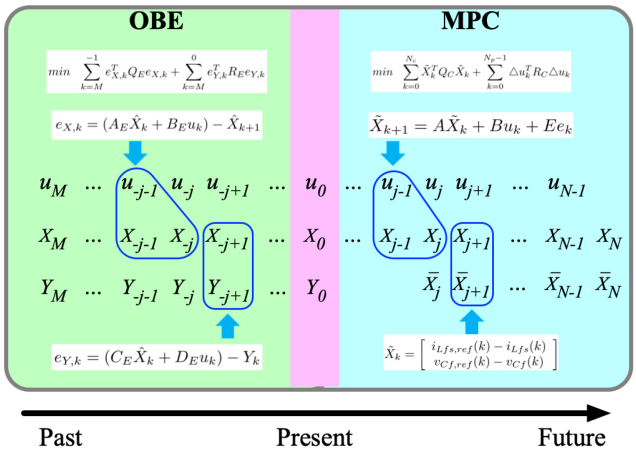

Fig. 5. Relationship between OBE and MPC.

Similar to the OBE implementation process, to achieve a high-frequency control and reduce the computation load of the DSP, the MPC problem is also solved explicitly by generating a piecewise affine feedback law. Figs. 3(b) and 4 show the specific implementing process of explicit MPC mechanism. The state-space model of (19) and constraints of the dynamic system are built offline to generate an online search tree and feedback law for the MPC optimization. In each controlling time period, the active region, s, is searched with the matrices $H_{s,c}$ and $K_{s,c}$. Then, in each of the specific active regions, the corresponding feedback law matrices, $F_{s,c}$ and $G_{s,c}$, are applied to calculate the optimal input values with the prediction horizon. Only the first value of the input sequence matrix is applied to the dynamic system for MPC control. Different colored regions in Fig. 3(b) represent various piecewise affine feedback low based on the estimated variables.

In every control time period, a binary search tree can find the optimal duty cycle based on the updated state values of inductor current/output voltage. Explicit MPC avoids the time-consuming online optimization process, thus it is suitable for high-frequency control. For a clearer form of display, the colored areas of the generated piecewise affine region block with the state variables of i_{Lfs}, v_{Cf}, and i_{Lfo} in Fig. 3(b) represent the n regions for MPC to search and optimize according to the feedback law. Specifically, the matrices $H_{s,c}$ and $K_{s,c}$ will lead to an active region. The corresponding matrices $F_{s,c}$ and $G_{s,c}$ will help calculate the optimal duty cycle for the PWM signals.

The working mechanisms of OBE and MPC are symmetrical with respect to the present state. Specifically, OBE is dealing with the states from past to present steps and MPC is optimizing the states from present to the future steps. The relationship between OBE and MPC has been shown in Fig. 5.

IV. OBE-MPC for DC/DC, DC/AC Grid and Motor Applications

With the basic LC power module in Fig. 1, the proposed integrated OBE-MPC technique can be applied to each of the power unit, as shown in Fig. 2, to build the software-defined power electronics architecture and enable a wide range of applications. Thus, a different number of the power modules combined with

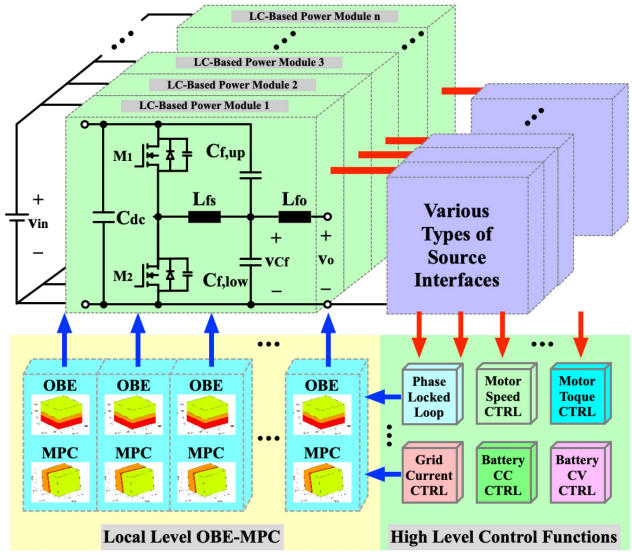

Fig. 6. Software-defined OBE-MPC power module-based power electronics architecture interfaced with wide applications.

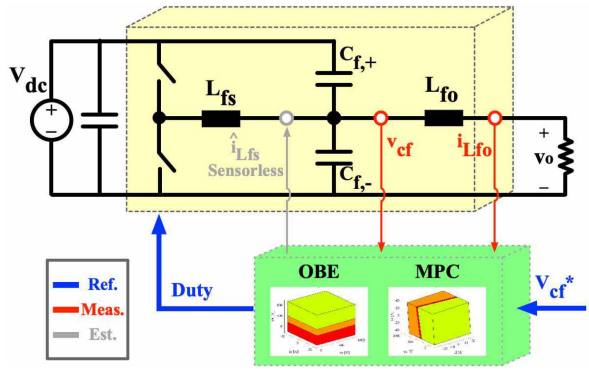

Fig. 7. Integrated OBE and MPC control diagram for the dc/dc interfaced application with LC-based power module.

the OBE-MPC algorithms can be reconfigured in Fig. 6 as desired circuitry topologies for various application purposes, e.g., single/three-phase dc/ac inverters, motor traction inverter, multiphase dc/dc converters to reduce the sensor cost, sampling noise and improve the dynamic performance. As shown in Fig. 6, the software-defined OBE-MPC power module-based power electronics architecture is composed of high-level control functions and local-level OBE-MPC function. The high-level control functions mainly include the holistic control algorithms for different applications. The local-level OBE-MPC functions is the algorithm designed in this article for each of the LC-based power module.

A. Dc/dc Application

The first application for the developed OBE-MPC technique is dc/dc interfaced power converter, as shown in Fig. 7. The combined OBE-MPC algorithms are configured in the LC-based power module to control the output voltage v_o. Specifically, the output capacitor voltage v_{Cf}, and output currenti_o, are directly measured as the output variable matrix Y_k, in (6). The inductor current $\hat{i_L}$, output capacitor voltage $\hat{v_{Cf}}$, and output current $\hat{i_o}$,

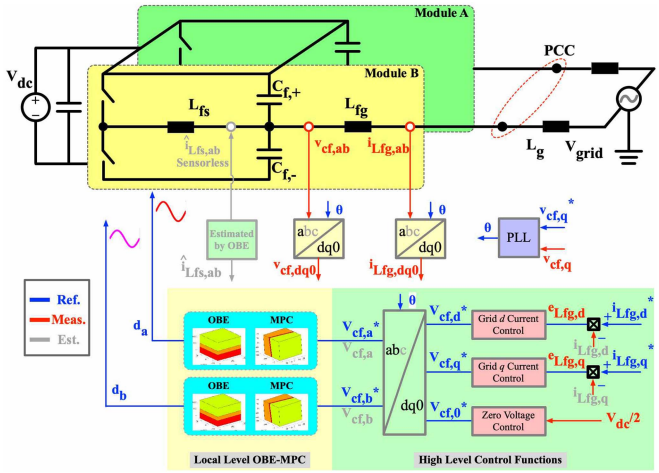

Fig. 8. Integrated OBE and MPC control diagram for the dc/ac single-phase interfaced application with LC-based power modules.

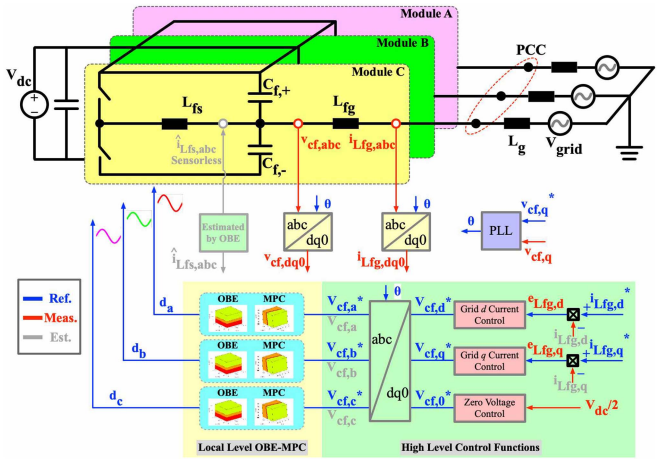

Fig. 9. Integrated OBE and MPC control diagram for the dc/ac three-phase interfaced application with LC-based power modules.

are configured as the estimated state variable matrix $\hat{X}_k$. Based on the OBE cost function in (10) and the corresponding constraints in (11)–(15) to deal with the past sampling information within the estimation horizon, the optimal estimation of $\hat{X}_k$ will be derived for the purpose of MPC control process with less noise.

Symmetrically with OBE, the MPC manages the future sampling information within the prediction horizon to derive the optimal input variable matrix u_k, of duty cycle by solving the MPC cost function in (22) and the corresponding constraints in (23)–(27). Instead of using the noisy sampling state variables of X_k, the MPC utilizes the estimated state variables $\hat{X}_k$, from OBE to track the output capacitor voltage reference with less noise and oscillation.

B. Dc/ac Application

The second application for the developed OBE-MPC is dc/ac interfaced power converters. As shown in Figs. 8 and 9, the OBE-MPC equipped LC-based power modules can be reconfigured as single/three-phase grid-connected inverters with two/three power modules, respectively.

1) Single-Phase Grid: For the dc/ac single-phase inverter and the corresponding control diagram in Fig. 8, the OBE-MPC algorithms are configured for each of the two LC-based power modules. Similarly with the dc/dc control diagram of Fig. 7, the OBE derives the estimation of three variables, inductor current $\hat{i_L}$, output capacitor voltage $\hat{v_{Cf}}$, and grid current $\hat{i_g}$, for MPC control process to achieve less noise, reduced sensor count and improved dynamic performance. The outer loop grid current control is implemented in $dq0$ reference frame with PI controllers to track the specific d and q components of the single-phase grid current $i^*_{g,d}$ and $i^*_{g,q}$, respectively. Then the outer loop grid current controller exports the d and q components of the output capacitor voltage references, $v^*_{Cf,d}$ and $v^*_{Cf,q}$, for the inner loop per phase power module OBE-MPC implementation. Since the inner loop OBE-MPC algorithm is implemented in the ab reference frame for each phase, the Park/Clarke transformations are inserted between the outer and inner loops to convert and allocate the output capacitor voltage references from $dq0$ to ab frame as $v^*_{Cf,a}$ and $v^*_{Cf,b}$ for the two phases of single-phase inverter application. In addition to the dq components, the zero-sequence control branch is also configured to control the zero-sequence capacitor voltage as half of the dc bus voltage, $v_{\rm dc}/2$, to stabilize the common mode voltage and attenuate the leakage current from flowing into the single-phase grid in the nonisolated circuit topology.

2) Three-Phase Grid: For the dc/ac three-phase inverter and the corresponding OBE-MPC control diagram in Fig. 9, the control principle is similar with the single-phase inverter application. Instead of two LC-based power modules, three power modules with the corresponding OBE-MPC algorithms are constructed to be interfaced with a three-phase grid for higher power capability. The outer loop grid current control is also implemented in $dq0$ reference frame with PI controllers to track the specific d and q components of the three-phase grid current, $i^*_{g,d}$ and $i^*_{g,q}$, respectively. Then the outer loop grid current controller exports the d and q components of the output capacitor voltage references, $v^*_{Cf,d}$ and $v^*_{Cf,q}$, for the inner loop per phase power module OBE-MPC implementation. Since the inner loop OBE-MPC algorithm is implemented in the abc reference frame for each phase, the Park/Clarke transformations are inserted between the outer and inner loops to convert and allocate the output capacitor voltage references from $dq0$ to abc frame as $v^*_{Cf,a}$, $v^*_{Cf,b}$ and $v^*_{Cf,c}$ for the three phases of three-phase inverter application. In addition to the dq components, the zero-sequence control branch is also configured to control the zero-sequence capacitor voltage as half of the dc bus voltage, $v_{dc}/2$, to stabilize the common mode voltage and attenuate the leakage current from flowing into the three-phase grid in the nonisolated circuit topology.

To conclude for both of the single/three-phase dc/ac grid applications, the OBE contributes to the noise attenuation from the sampling ADC data and cost reduction on sensor count. The MPC improves the dynamic performance with higher tracking speed and less oscillation due to the increased control bandwidth enabled by the inner loop MPC. Also, the developed cascaded

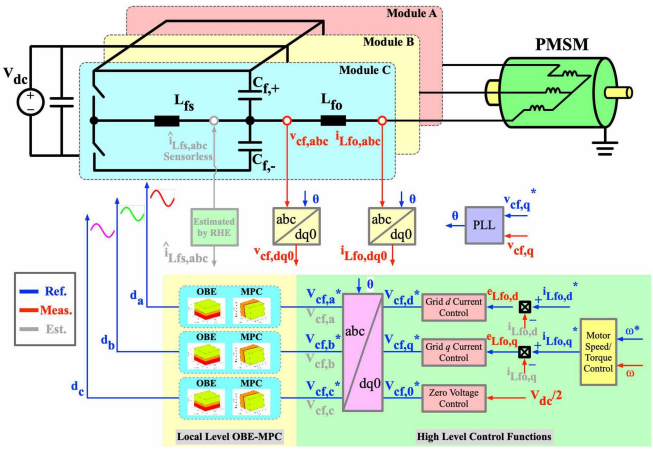

Fig. 10. Integrated OBE and MPC control diagram for the dc/ac motor interfaced application with LC-based power modules.

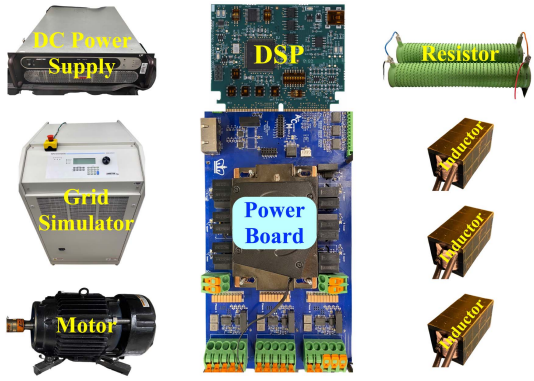

Fig. 11. Test bench for the implementation of OBE-MPC algorithms.

control architecture does not leverage the grid side inductor for MPC parametric modeling. This strategy avoids the unexpected MPC modeling parametric error from the interfaced grid caused by the unknown grid side equivalent inductance. Thus, the accuracy is further improved.

C. Motor Application

The third application for the developed OBE-MPC is the motor drive. As shown in Fig. 10, three of the OBE-MPC equipped LC-based power modules can be configured as motor traction inverter. The control diagram can be divided into three cascaded loops:

1) outer loop motor speed control;
2) middle loop motor current control; and
3) inner loop OBE-MPC control.

The outer loop speed controller is cascaded on top of the middle loop motor current q component controller to regulate the motor speed, ω with the desired reference, ω^*. Then, the middle loop motor current controller exports the d and q components of the output capacitor voltage references, $v^*_{Cf,d}$ and $v^*_{Cf,q}$, for the inner loop per phase power module OBE-MPC implementation. Since the inner loop OBE-MPC algorithm is also implemented in the abc reference frame for each phase, the Park/Clarke transformations are inserted between the middle and inner loops to convert and allocate the output capacitor voltage references from $dq0$ to abc frame as $v^*_{Cf,a}$, $v^*_{Cf,b}$, and $v^*_{Cf,c}$ for the three phases of the motor application. In addition to the dq components, the zero-sequence control branch is also configured for the motor traction inverter to control the zero-sequence capacitor voltage as half of the dc bus voltage, $v_{\rm dc}/2$, to stabilize the shaft voltage and attenuate the bearing current. With the zero-sequence stabilization, the possibility of motor failure can be reduced accordingly with less oscillation on shaft voltage and bearing current.

The studied topologies for the applications of dc/dc, dc/ac, and motor interfaces are equivalent to the general ones to implement the proposed OBE-MPC algorithms. The upper and lower output capacitors in Fig. 1 are functioned as the LC filtering for output current and voltage. The equivalent capacitance for output filtering is the same as the conventional topology by adding the upper/lower capacitance together. Thus, even though the number of capacitors is doubled, the total capacitance utilization is not sacrificed.

V. Merits and Validation

The OBE-MPC algorithms for the LC-based power modules are validated experimentally in this section for various applications, e.g., dc/dc converter, single/three-phase grid-connected inverters. The test bench is shown in Fig. 11, including the power board, control card, inductors, ac grid simulator, dc power supply, and resistor. The power switches are C3M0032120K SiC MOSFETs from CREE. The DSP controller is F280049C controlCARD from TI.

The merits of the developed OBE-MPC can be concluded in the following six aspects:

1) less sensor count by OBE for low cost;
2) lower noise by OBE for more stable control performance;
3) better dynamic performance by MPC for more robust transient;
4) less computation burden by the explicit implementation of OBE-MPC on a low-cost DSP;
5) wide applications with the OBE-MPC algorithms on the generalized LC-based power module; and
6) accurate state-space parametric modeling of OBE-MPC for LC-based power module without the influence of uncertainty and error from the output side interfaced unknown inductance.

The switching frequency and sampling frequency are both configured as 80 kHz. The control frequency is set as 20 kHz. In each control period, the sampled state variables are averaged with a factor of 4 to filter out the circuitry noise for better control performance.

A. Steady-State Performance of OBE-MPC

The steady-state performance of OBE-MPC is demonstrated in this section to show the noise/oscillation reduction and estimation accuracy of OBE and the tracking accuracy of MPC. Specifically, Fig. 12 shows the output current, capacitor voltage, and inductor current waveforms of the dc/dc converter with

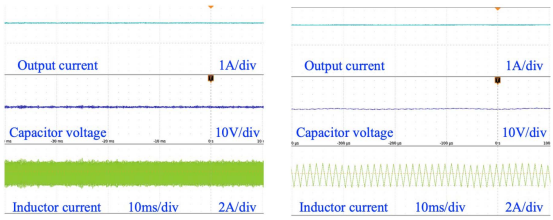

Fig. 12. OBE-MPC (a) experimental and (b) zoomed waveforms of output current, capacitor voltage, inductor current for dc/dc converter.

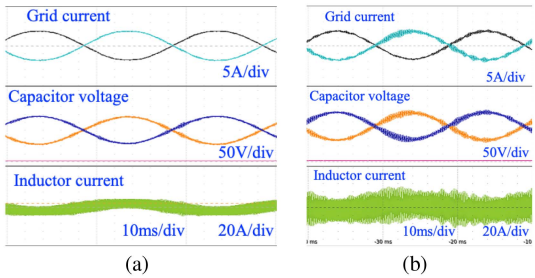

Fig. 13. Experimental waveforms of grid-interfaced single-phase dc/ac inductor current, capacitor voltage, grid current, and the dc bus voltage for MPC control (a) combined with OBE and (b) without OBE.

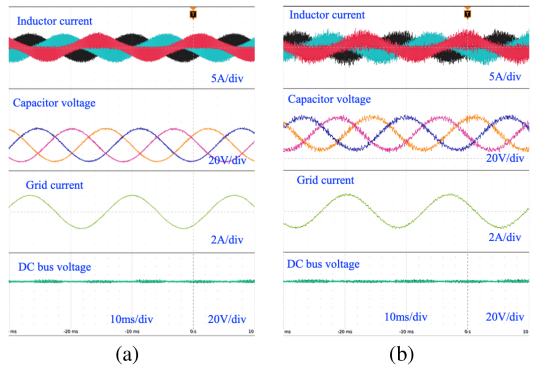

Fig. 14. Experimental waveforms of grid-interfaced three-phase dc/ac inductor current, capacitor voltage, grid current, and the dc bus voltage for MPC control (a) combined with OBE and (b) without OBE.

OBE-MPC method. Fig. 13(a) and (b) compare the grid current, output capacitor voltage, and inductor current of single-phase grid-interfaced dc/ac converter with and without OBE, respectively. Also, Fig. 14(a) and (b) shows the comparison with and without OBE for the three-phase grid dc/ac inverter, respectively. Both of the grid-connected applications demonstrate that OBE can reduce the noise and oscillation.

Furthermore, for the dc/dc application, the experimentally captured ADC readings of measurement and estimation for inductor current, capacitor voltage, and output current are shown in Fig. 15. Fig. 16 shows the MPC reference and measurement for dc/dc converter output capacitor voltage where the MPC accurately tracks a voltage reference of 50 V. For the grid interfaced application, the experimentally captured ADC readings of measurement and estimation for inductor current, capacitor voltage, and grid current are shown in Fig. 17. The sampling

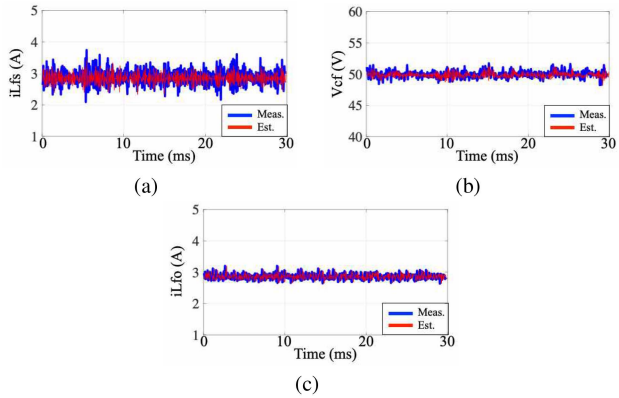

Fig. 15. OBE estimation performance of the experimentally captured steady-state ADC readings of measurement and estimation for dc/dc application (a) inductor current, (b) capacitor voltage, and (c) output current.

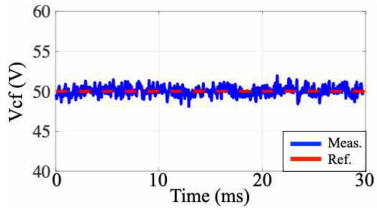

Fig. 16. MPC tracking performance of the experimentally captured steady-state ADC readings of capacitor voltage for the dc/dc application.

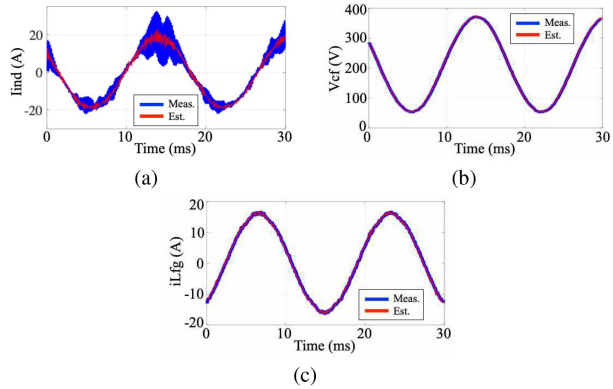

Fig. 17. OBE estimation performance of the experimentally captured steady-state ADC readings of measurement and estimation for grid-interfaced (a) inductor current, (b) capacitor voltage, and (c) grid current.

noise from the sensor is largely reduced by OBE for a more stable performance. And the estimation accuracy is high with a relatively low estimation error, as shown in Fig. 18. Fig. 19(a) and (b) shows the MPC references and measurement for grid q current and output capacitor voltage which demonstrate the high tracking accuracy of MPC.

For the influence of the parasitic circuit on the control accuracy, the predesigned parasitic resistor, and capacitor, R_{para} and C_{para}, are manually connected between the dc bus terminal and the neutral point of the grid simulator. The values of the R_{para} and C_{para} are selected based on the typical parasitic range between the automotive and photovoltaic systems. The corresponding control accuracy with different values of R_{para} and C_{para} has

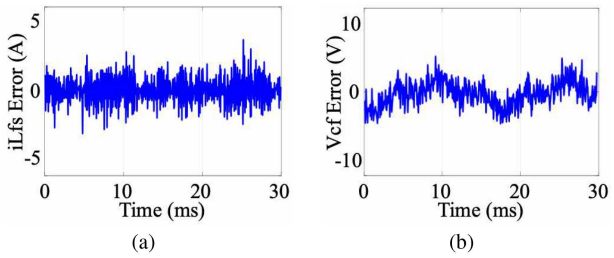

Fig. 18. OBE performance of the experimentally captured ADC readings of the estimation errors for grid-interfaced (a) inductor current and (b) capacitor voltage.

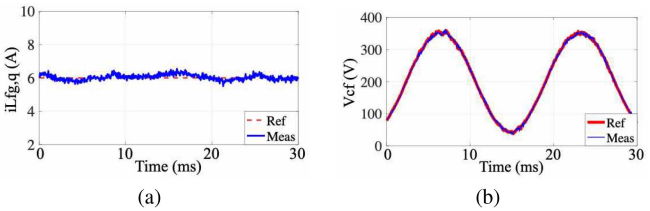

Fig. 19. MPC tracking performance of the experimentally captured steady-state ADC readings of measurement and reference for grid-interfaced (a) grid q current at 6 A and (b) capacitor voltage.

TABLE I
INFLUENCES OF PARASITIC VALUES ON TRACKING ACCURACY

R_{para} [Ω]	C_{para} [nF]	Tracking error
40	400	0.75%
30	300	0.55%
20	200	0.64%
10	100	0.83%
5	50	0.79%

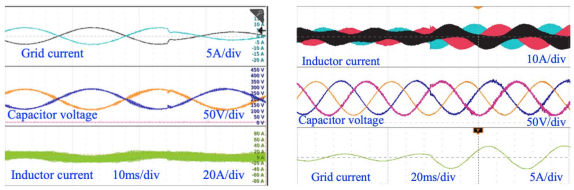

Fig. 20. Transient performance of the experimental inductor current, output capacitor voltage, and grid current waveforms for grid-interfaced applications of (a) single-phase dc/ac inverter with grid current step from 8 to 4 A and (b) three-phase dc/ac inverter with grid current step from 4 to 10 A.

been shown in Table I. It can be demonstrated that the parasitic values have limited influence on the control accuracy.

B. Transient Performance of OBE-MPC

The transient performance of OBE-MPC is demonstrated in this section to show the noise/oscillation reduction and estimation accuracy of OBE and the tracking accuracy and dynamic performance of MPC. Specifically, Fig. 20(a) and (b) shows the single- and three-phase grid-interfaced inverters grid current, output capacitor voltage, and inductor current transient waveforms with current steps from 8 to 2 A and 2 to 10 A, respectively. For the application of dc/dc converter, Fig. 21 captures the

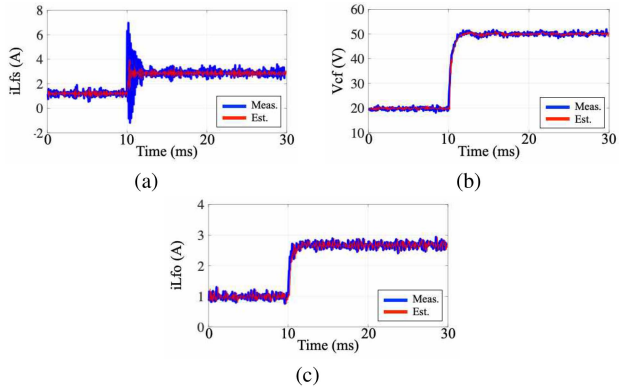

Fig. 21. OBE estimation performance of the experimentally captured transient ADC readings of measurement and estimation with a voltage step from 20 to 50 V for dc/dc application (a) inductor current, (b) capacitor voltage, and (c) output current.

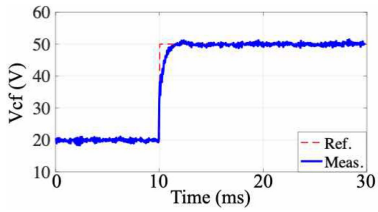

Fig. 22. MPC tracking performance of the experimentally captured transient ADC readings of capacitor voltage with a step from 20 V to 50 V for the dc/dc application.

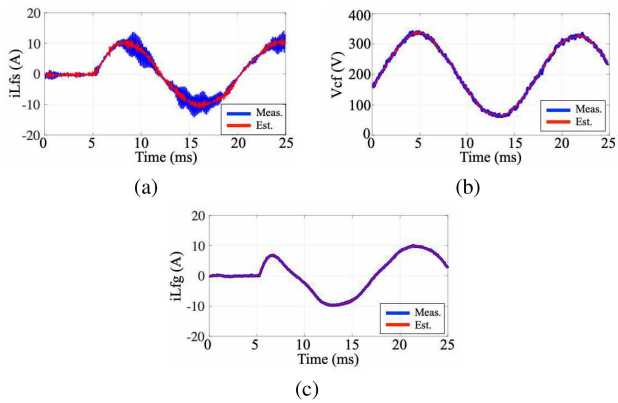

Fig. 23. OBE estimation performance of the experimentally captured transient ADC readings of measurement and estimation with a current step of 10 A for grid-interfaced (a) inductor current (b) capacitor voltage and (c) grid current.

experimental ADC readings of measurement and estimation for inductor current, output capacitor voltage, and output current with a voltage step from 20 to 50 V. The OBE can accurately estimate the measurements with less noise/oscillation, especially during the transient. Fig. 22 performs the experimental ADC readings of capacitor voltage measurement and the corresponding MPC reference with a step of 30 V. The MPC tracks the reference steadily within 2 ms. Furthermore, Fig. 23 captures the experimental ADC readings of measurement and estimation for grid-interfaced inverter inductor current, output capacitor voltage, and grid current with a current step from 0 to 10 A.

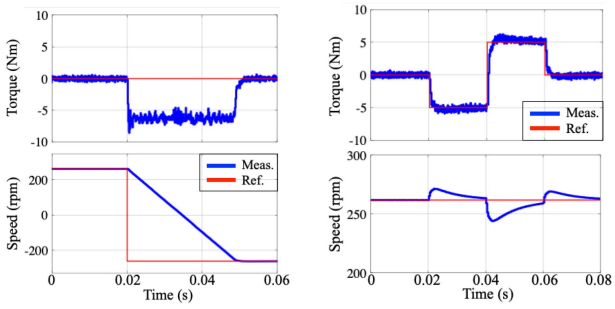

Fig. 24. OBE-MPC for the motor drive application with (a) speed step from 260 to −260 rpm and (b) torque step from −5 to 5 Nm.

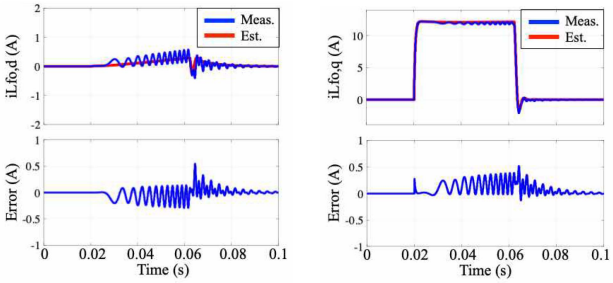

Fig. 25. OBE-MPC comparison between estimation and measurement and the corresponding estimation error for motor drive application of (a) $i_{Lfo,d}$ and (b) $i_{Lfo,q}$ currents with speed step transient.

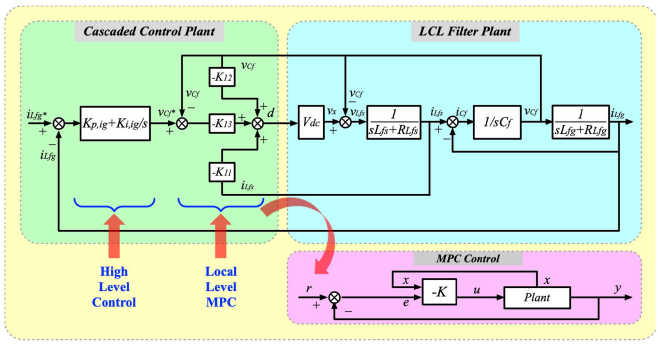

Fig. 26. Holistic diagram of cascaded MPC control and plant model.

The OBE can accurately estimate the measurements with less noise/oscillation during the transient. Fig. 24 demonstrates the motor drive application of the OBE-MPC with a speed step from 260 to -260 rpm in Fig. 24(a) and a torque step from -5 to 5 Nm in Fig. 24(b), respectively. Also, the measured and estimated dq components of the switch side inductor currents and the corresponding errors for motor application have been shown in Fig. 25.

C. Robustness and Stability of Control

The robustness and stability of the control performance are demonstrated in this section. For the proposed multilevel control method, the corresponding control, and system plant model have been shown in Fig. 26. The local level per phase switch side LC MPC is cascaded with the high level of grid side inductor current control. A linear-quadratic regulator (LQR) can be applied to derive the transfer function for the MPC algorithm portion in the control plant model of Fig. 26 to solve the cost function.

The typical LQR control diagram integrated with a dynamic system is shown in the bottom block of Fig. 26 where x, y, u, r represent the state variable $[i_{Lfs}; v_{Cf}]$, output variable i_{Lfs}, input variable of duty cycle d, and tracking reference $i_{Lfs,\text{ref}}$, respectively. The core algorithm of MPC to calculate the optimal duty cycle is a linear coefficient matrix, -K, and the MPC equation to calculate the optimal duty cycle based on the tracking error and state variable can be expressed as:

$$d = -\mathrm{K}\begin{bmatrix} i_{Lfs} \\ v_{Cf} \\ v_{Cf,\text{err}} \end{bmatrix} = -[K_{11}, K_{12}, K_{13}]\begin{bmatrix} i_{Lfs} \\ v_{Cf} \\ v_{Cf,\text{err}} \end{bmatrix} \tag{28}$$

where $v_{Cf,\text{err}}$ is the tracking error of the MPC calculated as $v_{Cf,\text{ref}} - v_{Cf}$.

Thus, the local-level MPC can be expressed in the transfer function as Fig. 26. The transfer function from tracking error $v_{Cf,\text{err}}$, to the measurement v_{Cf}, of output capacitor voltage can be expressed as

$$G_{vCf\text{err}2vCf,\text{MPC}}(s) = \frac{-K_{13}G_{\text{LCL},vx2ig}(s)(sL_{fg}+R_{Lfg})(sL_{fs}+R_{Lfs})/V_{\text{dc}}}{\begin{Bmatrix}(sL_{fs}+R_{Lfs})+K_{11}[V_{\text{dc}}-G_{\text{LCL},vx2ig}(s)(sL_{fg}+R_{Lfg})]/V_{\text{dc}} \\ +K_{12}G_{\text{LCL},vx2ig}(s)(sL_{fs}+R_{Lfs})(sL_{fg}+R_{Lfg})/V_{\text{dc}} \\ -K_{13}G_{\text{LCL},vx2ig}(s)(sL_{fs}+R_{Lfs})(sL_{fg}+R_{Lfg})/V_{\text{dc}}\end{Bmatrix}}. \tag{29}$$

Furthermore, the transfer function from the reference $v_{Cf,\text{ref}}$, to the measurement v_{Cf}, of output capacitor voltage can be expressed as

$$G_{vCf\text{ref}2vCf,\text{MPC}}(s) = G_{vCf\text{err}2vCf,\text{MPC}}(s)/[1 + G_{vCf\text{err}2vCf,\text{MPC}}(s)]. \tag{30}$$

Based on (30) and the LCL plant model in Fig. 26, the transfer function from the reference of output capacitor voltage $v_{Cf,\text{ref}}$, to the measurement of grid side inductor current i_{Lfg}, can be derived as

$$G_{vCf\text{ref}2iLfg,\text{MPC}}(s) = G_{vCf\text{ref}2vCf,\text{MPC}}(s)/(sL_{fg} + R_{Lfg}). \tag{31}$$

Then, taking the high-level grid side inductor current PI control into consideration, the cascaded MPC transfer function from tracking error $i_{Lfg,\text{err}}$, to the measurement i_{Lfg}, of grid side inductor current can be expressed as

$$G_{iLfg\text{err}2iLfg,\text{MPC}}(s) = G_{vCf\text{ref}2iLfg,\text{MPC}}(s) \cdot G_{iLfg,\text{PI}}(s). \tag{32}$$

The cascaded MPC transfer function from tracking error of grid side inductor $i_{Lfg,\text{err}}$, to the measurement of output capacitor voltage v_{Cf}, can be expressed as

$$G_{iLfg\text{err}2vCf,\text{MPC}}(s) = G_{vCf\text{ref}2vCf,\text{MPC}}(s) \cdot G_{iLfg,\text{PI}}(s). \tag{33}$$

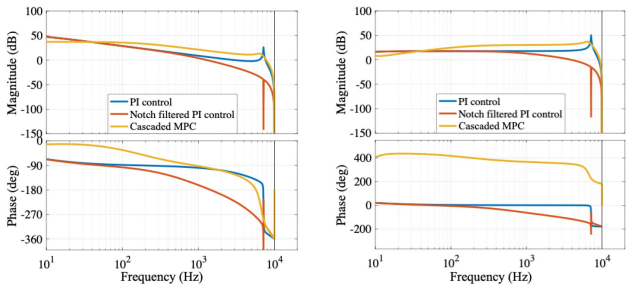

Fig. 27. Comparison of bode plots for the control strategies of conventional PI, notch filtered PI, and the proposed MPC (a) from $i_{Lfg,\mathrm{err}}$ to i_{Lfg} and (b) from $i_{Lfg,\mathrm{err}}$ to v_{Cf}.

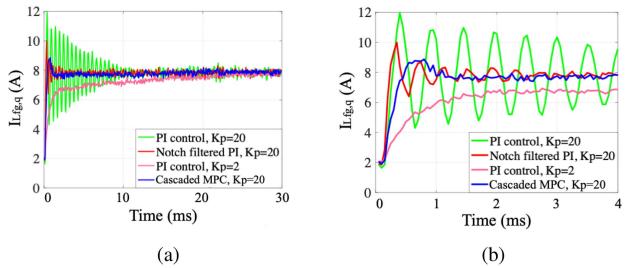

Fig. 28. Comparison of PI, notch filtered PI, and MMPC transient captured ADC readings of (a) grid side inductor current q component from 2 to 8 A and (b) zoomed waveforms.

The resonance behavior and dynamic performance of the three control strategies for LCL filtered grid-connected inverter are analyzed based on the derived transfer functions. Fig. 27(a) and (b) shows the bode plots comparison of transfer functions from the tracking error to the measurement of grid side inductor current and from the tracking error of grid side inductor current to the measurement of output capacitor voltage, respectively. The magnitude plots demonstrate that the conventional PI control has a convex spike at the resonant frequency point. The notch filtered PI control has a concave spike at the resonant frequency point. The developed cascaded MPC attenuates the spike at the resonant frequency point and the control bandwidth is wider than the conventional PI, notch filtered PI, and cascaded PI methods. The robustness and stability are improved correspondingly. For the dynamic performance comparison of PI control, notch filtered PI control, and cascaded MPC methods, Fig. 28 shows the $i_{Lfg,q}$ steps and zoomed waveforms from 2 to 8 A under the following four testing cases:

1) PI control with K_p gain of 20;
2) notch filtered PI control with K_p gain of 20;
3) PI control with K_p gain of 2;
4) cascaded MPC control with K_p gain of 20.

It can be seen that the proposed cascaded MPC behaves more stable than either PI control or notch filtered PI control at a high K_p gain of 20 with less overshoot and oscillation. Even though the PI method can act stably with a smaller K_p gain of 2, the response time is much longer than the proposed cascaded MPC method. Thus, the robustness and stability are improved with the cascaded MPC.

D. Comparison of OBE-MPC With Conventional Methods

The comparison between the proposed OBE-MPC with conventional estimation and control methods are analyzed in this section.

1) Control Comparison: For the control comparison with the conventional MPC methods, three aspects are demonstrated, including computation burden, parametric accuracy, and control performance. First, for the computation complexity, in the LCL filter inverter system, the conventional MPC methods typically require high-order state-space equations. The state-space matrix $\mathbf{A}$, is 9×9 in [31], 4×4 in [32], and 3×3 in [33], [34]. However, in the proposed MPC method, since only switch side LC filter parameters are necessary for the state-space formulation, the matrix order is reduced to be 2×2 in (20a). Thus, the online computation burden is reduced accordingly. The generated C code for the developed MPC algorithm is 5 KB, which is 2–3 times smaller than the third- and fourth-order state-space matrices systems. The execution time on the TI F280049C controlCARD is 4 μs, which is 2 times faster than the third-order state-space matrices systems. Second, for the parametric accuracy, since the developed control method is two-level multilayer architecture, the equivalent inductance and resistance from the output side interfaced applications will not influence the MPC parametric modeling of the LC-based power module. Thus, the accuracy of the MPC can be guaranteed without being affected by the uncertainty of the interfaced output inductance. However, for the conventional MPC methods with LCL converters in [31], [32], [33], [34], both the switch side and output side inductance values are required for the parametric modeling, which may result in error caused by the unknown output impedance. Third, for the control performance, the proposed method achieves the overshoot, rise/fall time, and practical bandwidth ($0.35/T_{\mathrm{rise}}$) of $\leq$10%, $\leq$1 ms, and $\geq$800 Hz. The overshoot, rise/fall time, and practical bandwidth in the conventional methods are 20%, 4 ms, 100 Hz for [35], 5%, 5 ms, 80 Hz for [36], and 3%, 20 ms, 20 Hz for [37].

2) Estimation Comparison: For the estimation compared with the conventional methods, four aspects are demonstrated, including noise reduction, estimation error, parametric accuracy, and sensor count. First, for the noise reduction, the extended state observer estimation method in [38] requires a digital filter to attenuate the noise from the measured and estimated values. A reduced order generalized parameter estimation-based observer is presented in [39] for the estimation of state variables. The system noise can be attenuated by increasing the filter gain λ, but the transient performance will be sacrificed. The disturbance-based estimation method reported in [40] is shown to be affected by Gaussian random noise on the output voltage side. The developed OBE reduces the noise by 60% and 25% on the switch side inductor current and output capacitor voltage, which demonstrates the noise reduction capability. Third, for the parametric accuracy, similarly to the MPC modeling, since the OBE is configured in each of the local-level power modules of the multilayer control/estimation structure, the equivalent inductance and resistance from the output side interfaced applications will not influence the OBE parametric modeling of the LC-based

TABLE II
MERITS SUMMARY OF OBE AND MPC

	Inductor current, I_{ind}	Capacitor voltage, V_{cap}
OBE noise reduction	60%	25%
OBE estimation error	3.2%	1.3%
MPC tracking error	2.4%	1.1%
MPC rise time	1.5 ms	2 ms
Conventional PI rise time	15 ms	23 ms
	File size	Execution time
Generated OBE C code	10 KB	7.12 μs
Generated MPC C code	5 KB	4.04 μs
Conventional PI C code	1 KB	1.04 μs

power module. Thus, the accuracy of the OBE can be guaranteed without being affected by the uncertainty of the interfaced output inductance. However, the conventional estimation methods for the application of LCL filtered converters require the unknown output side inductance, which may result in an error caused by the unknown output impedance [38], [39]. Finally, for the sensor count, the conventional control methods in [31], [32], [33], [34] require all the switch side current, output capacitor voltage, and output side current sensors to achieve the targets. The conventional estimation algorithm in [38] is based on the measurement of switch side inductor current value in single-phase LCL filter inverter with one current sensor. Kukkola et al. [41] and Kukkola and Hinkkanen [42] utilize the grid voltage and switch side inductor current sensors to estimate the output voltage for control. Awal et al. [43] leverage either the switch or grid side inductor current sensor along with the grid voltage sensor to perform active damping for LCL converter. Errouissi and Al-Durra [44] have designed the disturbance observer with the measurements of grid side inductor current and grid voltage sensors to estimate the switch side inductor current and output capacitor voltage values. The proposed OBE-MPC for each power module uses output side inductor current and output capacitor voltage sensors to optimally estimate the switch side inductor current, output capacitor voltage, and output side inductor current for control purposes.

The comparison among OBE, MPC, and the conventional PI control in noise reduction, estimation/tracking error, rise time, C code size, and execution time has been summarized in Table II to show the merits of the designed algorithms.

VI. CONCLUSION

This article develops a combined OBE-MPC technique for the software-defined LC power module-based power electronics architecture that can be leveraged for wide applications, e.g., dc/dc converters, single/three-phase dc/ac grid-connected inverters, and motor traction inverter. With the OBE, the sensor count is reduced with lower cost, and the sampling noise is attenuated with more stable control performance. With the MPC, the dynamic performance is improved with faster tracking speed and a more robust transient. The explicit implementation of OBE-MPC relieves the computation burden and enables the application on low-cost DSP. Different numbers of the OBE-MPC LC-based power modules are reconfigured to satisfy various load/source requirements and achieve highly accurate parametric modeling without being influenced by the unknown output inductance. The experiments have validated the developed algorithms and control architectures.

REFERENCES

[1] A. Moulichon et al., "Observer-based current controller for virtual synchronous generator in presence of unknown and unpredictable loads," *IEEE Trans. Power Electron.*, vol. 36, no. 2, pp. 1708–1716, Feb. 2021.

[2] Z. Dai, W. Lin, and H. Lin, "Estimation of single-phase grid voltage parameters with zero steady-state error," *IEEE Trans. Power Electron.*, vol. 31, no. 5, pp. 3867–3879, May 2016.

[3] S. Zhu et al., "Robust speed control of electrical drives with reduced ripple using adaptive switching high-order extended state observer," *IEEE Trans. Power Electron.*, vol. 37, no. 2, pp. 2009–2020, Feb. 2022.

[4] T. V. Tran, K.-H. Kim, and J.-S. Lai, "Optimized active disturbance rejection control with resonant extended state observer for grid voltage sensorless LCL-filtered inverter," *IEEE Trans. Power Electron.*, vol. 36, no. 11, pp. 13317–13331, Nov. 2021.

[5] Z. Yin, C. Bai, N. Du, C. Du, and J. Liu, "Research on internal model control of induction motors based on Luenberger disturbance observer," *IEEE Trans. Power Electron.*, vol. 36, no. 7, pp. 8155–8170, Jul. 2021.

[6] Q. Ouyang, J. Chen, and J. Zheng, "State-of-charge observer design for batteries with online model parameter identification: A robust approach," *IEEE Trans. Power Electron.*, vol. 35, no. 6, pp. 5820–5831, Jun. 2020.

[7] A. Alessandri, M. Baglietto, and G. Battistelli, "Receding-horizon estimation for switching discrete-time linear systems," *IEEE Trans. Autom. Control*, vol. 50, no. 11, pp. 1736–1748, Nov. 2005.

[8] K. Ling and K. Lim, "Receding horizon recursive state estimation," *IEEE Trans. Autom. Control*, vol. 44, no. 9, pp. 1750–1753, Sep. 1999.

[9] W. Xu, R. Dian, Y. Liu, D. Hu, and J. Zhu, "Robust flux estimation method for linear induction motors based on improved extended state observers," *IEEE Trans. Power Electron.*, vol. 34, no. 5, pp. 4628–4640, May 2019.

[10] Z. Yin, Y. Zhang, C. Du, J. Liu, X. Sun, and Y. Zhong, "Research on anti-error performance of speed and flux estimation for induction motors based on robust adaptive state observer," *IEEE Trans. Ind. Electron.*, vol. 63, no. 6, pp. 3499–3510, Jun. 2016.

[11] J.-N. Shen, J.-J. Shen, Y.-J. He, and Z.-F. Ma, "Accurate state of charge estimation with model mismatch for Li-ion batteries: A joint moving horizon estimation approach," *IEEE Trans. Power Electron.*, vol. 34, no. 5, pp. 4329–4342, May 2019.

[12] C. Alfaro, R. Guzman, L. G. de Vicuña, J. Miret, and M. Castilla, "Dual-loop continuous control set model-predictive control for a three-phase unity power factor rectifier," *IEEE Trans. Power Electron.*, vol. 37, no. 2, pp. 1447–1460, Feb. 2022.

[13] Y. Zhang, Y. Peng, and H. Yang, "Performance improvement of two-vectors-based model predictive control of PWM rectifier," *IEEE Trans. Power Electron.*, vol. 31, no. 8, pp. 6016–6030, Aug. 2016.

[14] C. Buccella, C. Cecati, H. Latafat, P. Pepe, and K. Razi, "Observer-based control of LLC DC/DC resonant converter using extended describing functions," *IEEE Trans. Power Electron.*, vol. 30, no. 10, pp. 5881–5891, Oct. 2015.

[15] L. Zheng, R. P. Kandula, and D. Divan, "Robust predictive control for modular solid-state transformer with reduced DC link and parameter mismatch," *IEEE Trans. Power Electron.*, vol. 36, no. 12, pp. 14295–14311, Dec. 2021.

[16] Z. Zhang, F. Wang, T. Sun, J. Rodríguez, and R. Kennel, "FPGA-based experimental investigation of a quasi-centralized model predictive control for back-to-back converters," *IEEE Trans. Power Electron.*, vol. 31, no. 1, pp. 662–674, Jan. 2016.

[17] J. Holtz, "Predictive finite-state control–when to use and when not," *IEEE Trans. Power Electron.*, vol. 37, no. 4, pp. 4225–4232, Apr. 2022.

[18] Y. Yang, S.-C. Tan, and S. Y. R. Hui, "Adaptive reference model predictive control with improved performance for voltage-source inverters," *IEEE Trans. Control Syst. Technol.*, vol. 26, no. 2, pp. 724–731, Mar. 2018.

[19] X. Liu, D. Wang, and Z. Peng, "Cascade-free fuzzy finite-control-set model predictive control for nested neutral point-clamped converters with low switching frequency," *IEEE Trans. Control Syst. Technol.*, vol. 27, no. 5, pp. 2237–2244, Sep. 2019.

[20] M. Narimani, B. Wu, V. Yaramasu, Z. Cheng, and N. R. Zargari, "Finite control-set model predictive control (FCS-MPC) of nested neutral point-clamped (NNPC) converter," *IEEE Trans. Power Electron.*, vol. 30, no. 12, pp. 7262–7269, Dec. 2015.

[21] N. Panten, N. Hoffmann, and F. W. Fuchs, "Finite control set model predictive current control for grid-connected voltage-source converters with LCL filters: A study based on different state feedbacks," *IEEE Trans. Power Electron.*, vol. 31, no. 7, pp. 5189–5200, Jul. 2016.
[22] A. Monti and F. Ponci, "PEBB standardization for high-level control: A proposal," *IEEE Trans. Ind. Electron.*, vol. 59, no. 10, pp. 3700–3709, Oct. 2012.
[23] T. Ericsen, Y. Khersonsky, P. Schugart, and P. Steimer, "PEBB—power electronics building blocks, from concept to reality," in *Proc. 3rd IET Int. Conf. Power Electron., Mach. Drives*, 2006, pp. 12–16.
[24] A. Deshpande, Y. Chen, B. Narayanasamy, Z. Yuan, C. Chen, and F. Luo, "Design of a high-efficiency, high specific-power three-level t-type power electronics building block for aircraft electric-propulsion drives," *IEEE Trans. Emerg. Sel. Topics Power Electron.*, vol. 8, no. 1, pp. 407–416, Mar. 2020.
[25] H. L. Ginn, N. Hingorani, J. R. Sullivan, and R. Wachal, "Control architecture for high power electronics converters," *Proc. IEEE*, vol. 103, no. 12, pp. 2312–2319, Dec. 2015.
[26] Y. Li, Y. Gu, and T. Green, "Revisiting grid-forming and grid-following inverters: A duality theory," *IEEE Trans. Power Syst.*, to be published, doi: 10.1109/TPWRS.2022.3151851.
[27] X. Yu, A. M. Khambadkone, H. Wang, and S. T. S. Terence, "Control of parallel-connected power converters for low-voltage microgrid—Part I: A hybrid control architecture," *IEEE Trans. Power Electron.*, vol. 25, no. 12, pp. 2962–2970, Dec. 2010.
[28] H. Wang, A. M. Khambadkone, and X. Yu, "Control of parallel connected power converters for low voltage microgrid—Part II: Dynamic electrothermal modeling," *IEEE Trans. Power Electron.*, vol. 25, no. 12, pp. 2971–2980, Dec. 2010.
[29] P. Tøndel, T. A. Johansen, and A. Bemporad, "Evaluation of piecewise affine control via binary search tree," *Automatica*, vol. 39, no. 5, pp. 945–950, 2003.
[30] M. Herceg, M. Kvasnica, C. N. Jones, and M. Morari, "Multi-parametric toolbox 3.0," in *Proc. Eur. Control Conf.*, 2013, pp. 502–510.
[31] M. G. Judewicz, S. A. González, J. R. Fischer, J. F. Martínez, and D. O. Carrica, "Inverter-side current control of grid-connected voltage source inverters with LCL filter based on generalized predictive control," *IEEE Trans. Emerg. Sel. Topics Power Electron.*, vol. 6, no. 4, pp. 1732–1743, Dec. 2018.
[32] S. Mariethoz and M. Morari, "Explicit model-predictive control of a PWM inverter with an LCL filter," *IEEE Trans. Ind. Electron.*, vol. 56, no. 2, pp. 389–399, Feb. 2009.
[33] C. Xue, D. Zhou, and Y. Li, "Hybrid model predictive current and voltage control for LCL-filtered grid-connected inverter," *IEEE Trans. Emerg. Sel. Topics Power Electron.*, vol. 9, no. 5, pp. 5747–5760, Oct. 2021.
[34] R. Guzman, L. G. de Vicuña, A. Camacho, J. Miret, and J. M. Rey, "Receding-horizon model-predictive control for a three-phase VSI with an LCL filter," *IEEE Trans. Ind. Electron.*, vol. 66, no. 9, pp. 6671–6680, Sep. 2019.
[35] C. S. Lim, H. H. Goh, and S. S. Lee, "Long-prediction-horizon near-optimal model predictive grid current control for PWM-driven VSIs with LCL filters," *IEEE Trans. Power Electron.*, vol. 36, no. 2, pp. 2246–2257, Feb. 2021.
[36] N. N. Nam, N. D. Nguyen, C. Yoon, M. Choi, and Y. I. Lee, "Voltage sensorless model predictive control for a grid-connected inverter with LCL filter," *IEEE Trans. Ind. Electron.*, vol. 69, no. 1, pp. 740–751, Jan. 2022.
[37] N. N. Nam, N.-D. Nguyen, C. Yoon, and Y. I. Lee, "Disturbance observer-based robust model predictive control for a voltage sensorless grid-connected inverter with an LCL filter," *IEEE Access*, vol. 9, pp. 109793–109805, 2021.
[38] B. Wang, Y. Xu, Z. Shen, J. Zou, C. Li, and H. Liu, "Current control of grid-connected inverter with LCL filter based on extended-state observer estimations using single sensor and achieving improved robust observation dynamics," *IEEE Trans. Ind. Electron.*, vol. 64, no. 7, pp. 5428–5439, Jul. 2017.
[39] W. He, M. M. Namazi, T. Li, and R. Ortega, "A state observer for sensorless control of power converters with unknown load conductance," *IEEE Trans. Power Electron.*, vol. 37, no. 8, pp. 9187–9199, Aug. 2022.
[40] S. Zhuo, A. Gaillard, L. Xu, D. Paire, and F. Gao, "Extended state observer-based control of DC–DC converters for fuel cell application," *IEEE Trans. Power Electron.*, vol. 35, no. 9, pp. 9923–9932, Sep. 2020.
[41] J. Kukkola, M. Hinkkanen, and K. Zenger, "Observer-based state-space current controller for a grid converter equipped with an LCL filter: Analytical method for direct discrete-time design," *IEEE Trans. Ind. Appl.*, vol. 51, no. 5, pp. 4079–4090, Sep./Oct. 2015.
[42] J. Kukkola and M. Hinkkanen, "Observer-based state-space current control for a three-phase grid-connected converter equipped with an LCL filter," *IEEE Trans. Ind. Appl.*, vol. 50, no. 4, pp. 2700–2709, Jul./Aug. 2014.
[43] M. A. Awal, L. D. Flora, and I. Husain, "Observer based generalized active damping for voltage source converters with LCL filters," *IEEE Trans. Power Electron.*, vol. 37, no. 1, pp. 125–136, Jan. 2022.
[44] R. Errouissi and A. Al-Durra, "Design of PI controller together with active damping for grid-tied LCL-filter systems using disturbance-observer-based control approach," *IEEE Trans. Ind. Appl.*, vol. 54, no. 4, pp. 3820–3831, Jul./Aug. 2018.

Liwei Zhou (Member, IEEE) received the B.E. and the M.E.degrees from Shandong University, Jinan, China, in 2014 and 2017, respectively, and the Ph.D. degree from Columbia University, New York, NY, USA, in 2022, all in electrical engineering.

He is currently a Research Associate in Motor Drives and Power Electronics Laboratory, Columbia University. His current research interests include soft-switching techniques for modular power converter, model predictive control, state estimation and other advanced control technologies, grid-connected converter, electric vehicle battery charging control, and inductor design.

Dr. Zhou was the Session Chair in 2022 IEEE/AIAA ITEC+EATS. He was the recipient of the best paper award in the International Conference on Applied Energy, MIT A+B 2022. He was also the recipient of the IEEE Energy Conversion Congress and Expo 2018 Student Travel Award. He was also the co-recipient of the Best Student Paper Award of the IEEE Transportation Electrification Conference and Expo 2021.

Michael Eull (Member, IEEE) received the B.Eng.Mgt. and MASc degrees from McMaster University, Hamilton, ON, Canada and the Ph.D. degree from Columbia University, New York, NY, USA, all in electrical engineering.

He is currently a Research and Development Engineer in power electronics with the Power Networks Demonstration Centre, University of Strathclyde, Glasgow, U.K. His research interests include in estimation and control of power electronics and motor drives for transportation electrification.

Dr. Eull was the Treasurer for the 2022 IEEE/AIAA ITEC+EATS conference.

Matthias Preindl (Senior Member, IEEE) received the B.Sc. degree in electrical engineering (*summa cum laude*) from the University of Padua, Padua, Italy, the M.Sc. degree in electrical engineering and information technology from ETH Zurich, Switzerland, and the Ph.D. degree in energy engineering from the University of Padua, in 2008, 2010, and 2014, respectively.

He is currently an Associate Professor of Power Electronic Systems in the Department of Electrical Engineering at Columbia University, New York, NY, USA. Prior to joining Columbia University in 2016, he was an R&D Engineer of Power Electronics and Drives with Leitwind AG, Italy (2010–2012), a Postdoctoral Research Associate with the McMaster Institute for Automotive Research and Technology, McMaster University, Hamilton, ON, Canada (2014–2015), and a Sessional Professor in the Department of Electrical and Computer Engineering, McMaster University (2015). His research interests include the design and control of motor drives, power electronics, and batteries for transportation electrification and renewable energy.

Dr. Preindl was an Area Editor for IEEE TRANSACTIONS ON VEHICULAR TECHNOLOGY, Associate EiC of Springer Nature/China *SAE Journal of Automotive Innovation*, and as the General Chair of the 2022 IEEE/AIAA ITEC+EATS. He is a Fellow of IET, recipient of the Horiba Awards Honorable Mention (Japan, 2019), the Futura Foundation Award (Italy, 2017), and the NSF CAREER Award (USA, 2017), co-recipient of Fast Company's World Changing Ideas Awards honorable mention (co-recipient, USA, 2022) as well as best paper and presentation recognitions including the 2019 IEEE Transactions on Industrial Electronics best paper award.